

# The Infrared Camera (IRC) for *AKARI* - Design and Imaging Performance

Takashi ONAKA,<sup>1</sup> Hideo MATSUHARA,<sup>2</sup> Takehiko WADA,<sup>2</sup> Naofumi FUJISHIRO,<sup>3\*</sup>

Hideaki FUJIWARA,<sup>1</sup> Miho ISHIGAKI,<sup>4</sup> Daisuke ISHIHARA,<sup>1</sup> Yoshifusa ITA,<sup>2</sup>

Hirokazu KATAZA,<sup>2</sup> Woojung KIM,<sup>2</sup> Toshio MATSUMOTO,<sup>2</sup> Hiroshi MURAKAMI,<sup>2</sup>

Youichi OHYAMA,<sup>2</sup> Shinki OYABU,<sup>2</sup> Itsuki SAKON,<sup>1</sup> Toshihiko TANABÉ,<sup>5</sup>

Toshinobu TAKAGI,<sup>2</sup> Kazunori UEMIZU,<sup>2</sup> Munetaka UENO,<sup>6</sup> Fumio USUI,<sup>2</sup> Hidenori WATARAI,<sup>7</sup>

Martin COHEN,<sup>8</sup> Keigo ENYA,<sup>2</sup> Takafumi OOTSUBO,<sup>9</sup> Chris P. PEARSON,<sup>2,10</sup>

and

Norihide TAKEYAMA,<sup>11</sup> Tomoyasu YAMAMURO,<sup>11†</sup> Yuji IKEDA,<sup>11‡</sup>

<sup>1</sup>*Department of Astronomy, Graduate School of Science, The University of Tokyo,*

*Bunkyo-ku, Tokyo 113-0033, Japan*

*onaka@astron.s.u-tokyo.ac.jp*

<sup>2</sup>*Institute of Space and Astronautical Science,*

*Japan Aerospace Exploration Agency, Sagami-hara, Kanagawa 229-8510, Japan*

<sup>3</sup>*Department of Physics, Graduate School of Science, The University of Tokyo,*

*Bunkyo-ku, Tokyo 113-0033, Japan*

<sup>4</sup>*Department of Physics, Faculty of Science, Tokyo Institute of Technology,*

*Meguro-ku, Tokyo 15208551, Japan*

<sup>5</sup>*Institute of Astronomy, Graduate School of Science, The University of Tokyo,*

*Mitaka, Tokyo 181-0015, Japan*

<sup>6</sup>*Department of Earth Science and Astronomy, Graduate School of Arts and Sciences,*

*The University of Tokyo, Meguro-ku, Tokyo 153-8902, Japan*

<sup>7</sup>*Office of Space Applications, Japan Aerospace Exploration Agency,*

*Tsukuba, Ibaraki 305-8505, Japan*

<sup>8</sup>*Radio Astronomy Laboratory, 601 Campbell Hall, University of California,*

*Berkeley, CA 94720, U.S.A.*

<sup>9</sup>*Graduate School of Science, Nagoya University, Furo-cho, Chikusa-ku, Nagoya 464-8602, Japan*

<sup>10</sup>*ISO Data Center, European Space Agency, Villafranca del Castillo, P.B.Box 50727,*

*28080 Madrid, Spain*

<sup>11</sup>*Genesis Corporation, Shimo-renjaku, Mitaka, Tokyo 181-0013, Japan*

(Received 2007 March 2; accepted 2001 April 9)

## Abstract

The Infrared Camera (IRC) is one of two focal-plane instruments on the *AKARI*

satellite. It is designed for wide-field deep imaging and low-resolution spectroscopy in the near- to mid-infrared ( $1.8\text{--}26.5\,\mu\text{m}$ ) in the pointed observation mode of *AKARI*. IRC is also operated in the survey mode to make an all-sky survey at  $9$  and  $18\,\mu\text{m}$ . It comprises three channels. The NIR channel ( $1.8\text{--}5.5\,\mu\text{m}$ ) employs a  $512 \times 412$  InSb array, whereas both the MIR-S ( $4.6\text{--}13.4\,\mu\text{m}$ ) and MIR-L ( $12.6\text{--}26.5\,\mu\text{m}$ ) channels use  $256 \times 256$  Si:As impurity band conduction arrays. Each of the three channels has a field-of-view of about  $10' \times 10'$  and are operated simultaneously. The NIR and MIR-S share the same field-of-view by virtue of a beam splitter. The MIR-L observes the sky about  $25'$  away from the NIR/MIR-S field-of-view. IRC gives us deep insights into the formation and evolution of galaxies, the evolution of planetary disks, the process of star-formation, the properties of interstellar matter under various physical conditions, and the nature and evolution of solar system objects. The in-flight performance of IRC has been confirmed to be in agreement with the pre-flight expectation. This paper summarizes the design and the in-flight operation and imaging performance of IRC.

**Key words:** infrared: general – instrumentation: detectors – space vehicles: instruments

## 1. Introduction

The *AKARI* spacecraft may be fixed in inertial space for up to approximately 600s to make a pointed observation in addition to the continuous survey mode, in which all-sky survey observations are performed (Murakami et al. 2007). The Infrared Camera (IRC) on board *AKARI* is uniquely designed for deep imaging and spectroscopy for pointed observations, while it is also operated in the survey mode (Onaka et al. 2004).

Because of the nature of near-earth orbits, severe visibility constraints are imposed on pointed observations of *AKARI* (Murakami et al. 2007). The IRC is designed to maximize the observation efficiency in a pointed observation. It consists of three channels divided by the spectral range, each of which has a wide field-of-view of about  $10' \times 10'$  at the cost of the spatial resolution. The IRC is designed as a general-purpose instrument to obtain information on the spectral energy distribution of an object in the near- to mid-infrared. The imaging bands are selected to evenly cover the spectral range ( $1.8 - 26.5\,\mu\text{m}$ ) limited by the detector responses as much as possible. The IRC has a unique feature of slit-less spectroscopy to obtain spectra of multiple objects in a pointed observation for the first time in space-borne instruments

---

\* Present Address is Cybernet systems Co. Ltd., Bunkyo-ku, Tokyo 112-0012, Japan

† Present address: OptCraft, Hadano, Kanagawa, 259-1331, Japan

‡ Present address: Photocoding, Higashi-Hashimoto, Sagami-hara, Kanagawa, 229-1104, Japan

(Ohyama et al. 2007). The worth of imaging and low-resolution spectroscopy in the near- to mid-infrared has well been demonstrated by successful observations of ISOCAM on board the Infrared Space Observatory (Cesarsky et al. 1996). IRC has a much wider field-of-view and a longer wavelength coverage with fewer filter selections than the ISOCAM. Compared to the Infrared Array Camera (IRAC) on *Spitzer* (Fazio et al. 2004), IRC has a wider field-of-view with larger pixel scales and spectral coverage longer than  $10\ \mu\text{m}$ . The IRC also has a spectroscopic capability for wavelengths shorter than  $5\ \mu\text{m}$ , which the Infrared Spectrograph (IRS) on *Spitzer* does not cover (Houck et al. 2004). Small slits in the IRC enable spectroscopy for diffuse sources. IRC targets range from distant galaxies to solar system objects. The prime scientific themes include the formation and evolution of galaxies, the evolution of planetary disks, the process of star-formation, the properties of interstellar medium, and the nature of solar system objects, by means of deep imaging and spectroscopic surveys of wide areas of the sky (Matsuhara et al. 2005; Matsuhara et al. 2006).

This paper reports the basic design and the in-flight performance of IRC imaging observations. The performance in the spectroscopic mode is given separately in Ohyama et al. (2007). The data reduction of the all-sky observation mode is described in Ishihara et al. (2007). The in-flight calibration as well as the stability of the performance will be given in Tanabé et al. (in prep.)

## 2. Instrumentation Description

IRC consists of three channels: the NIR channel operates from  $1.8\text{--}5.3\ \mu\text{m}$ ; the MIR-S channel works in  $5.4\text{--}13.1\ \mu\text{m}$ ; and the MIR-L channel covers  $12.4\text{--}26.5\ \mu\text{m}$ . All three channels are operated simultaneously. The NIR employs a  $512 \times 412$  InSb array, whereas the MIR-S and MIR-L use  $256 \times 256$  Si:As arrays. The InSb array operates at about 10K and the Si:As arrays at 6.5–7K. To achieve these temperatures in a stable condition, the InSb array unit has a weak thermal connection to the focal-plane instrument (FPI) plate, whereas the MIR detector units are connected firmly to the plate. The FPI plate is weakly connected to the helium tank and is cooled by the evaporating helium gas to about 6 K (Nakagawa et al. 2007). The IRC arrays are kept running all the time and the temperatures of the arrays are kept stable by the balance between their self-heating and the cooling to the FPI plate. The heat dissipation is approximately 0.6 mW per array. Both arrays were supplied by Raytheon, California, U.S.A. The Si:As arrays are of the same type as those employed by IRAC on *Spitzer* (Fazio et al. 2004), while the InSb array is a larger format version of those on IRAC. All three channels use refractive optics to enable a compact design and achieve a nearly diffraction-limited performance. The final image quality is dominated by the wave-front errors of the telescope for the NIR channel (Kaneda et al. 2007). Each channel is equipped with three filters for imaging observations, two dispersive elements (prism and grisms) for spectroscopic observations, and the shutter for the dark measurement, all of which are installed in the filter wheel with a

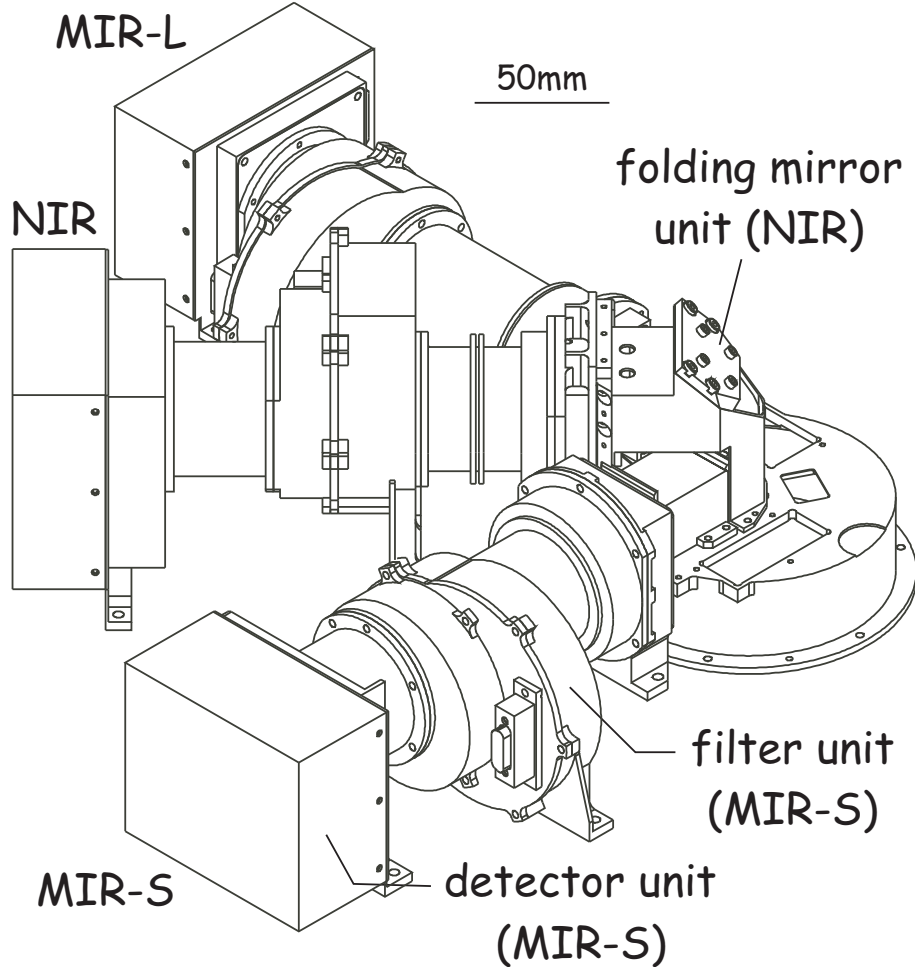


**Fig. 1.** Bird's-eye view of the IRC.

stepping motor and each of which is selected by rotating the wheel. The stepping motor was specially developed for cryogenic applications by Sumitomo Heavy Industry. The filter wheel mechanism has extensively been tested on the ground and has never failed so far. It allows us to make multi-filter observations and the measurement of dark current in one pointing. The photometric band and disperser parameters are summarized in Table 1. A bird's-eye view of the IRC is shown in Figure 1. Figure 2 shows a photograph of the IRC installed on the focal plane.

Figure 3 shows the layout of the fields-of-view of each IRC channel. The NIR and MIR-S share the same field-of-view by virtue of the beam splitter. The MIR-L has a field-of-view at  $25'$  away from that of the NIR/MIR-S, taking account of the focal-plane curvature. The dispersers are all of transmission type and thus IRC spectroscopic observations can be carried out in a slit-less mode. In addition, every channel has a small slit area as shown in Figure 3 and slit-spectroscopy can also be performed. These slits are installed in the field stops at the telescope focal plane as shown in figure 4. The NIR detector array has an extra part of  $100 \times 412$  pixels

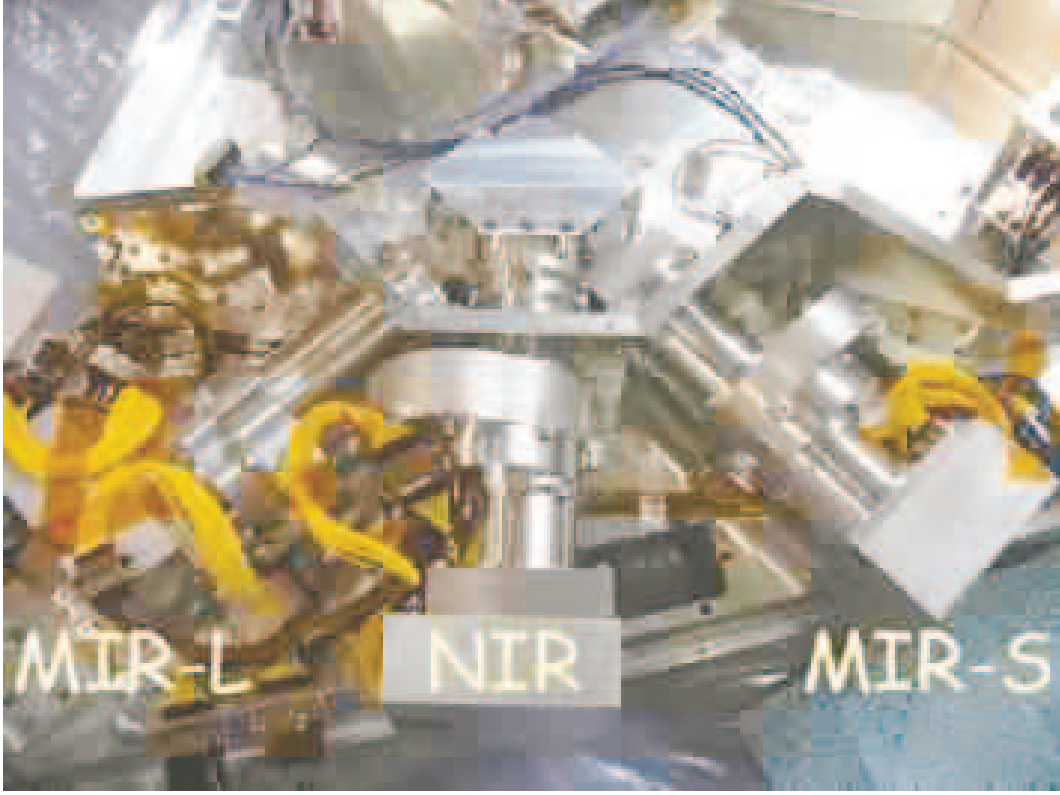


**Fig. 2.** Photograph of the IRC on the FPI plate with the telescope behind the plate. From left to right, MIR-L, NIR, and MIR-L.

in addition to the square area, which provides an extra slit area. The NIR slit consists of a wide part in the middle ( $1' \times 1'$ ), which is used for spectroscopy of point sources with the grism (NG) to avoid confusion with nearby sources, and the narrow parts at the left and right are used for spectroscopy of diffuse sources. The left part ( $5'' \times 0.4'$ ) is shared with the MIR-S. The small slit of the MIR-L is located at the opposite side of the field-of-view compared to the NIR and MIR-S channels and is also designed for spectroscopy of diffuse sources. The absolute accuracy of the telescope pointing is generally better than  $3''$ . This is sufficient to place a point source in the large  $1' \times 1'$  slit for NIR. Details of the mechanical design are given in Watarai et al. (2000). IRC weighs approximately 3.9kg in total, including the focal-plane interface nicknamed “Swiss cheese”, which has many holes for the field stops.

Figure 4 depicts the optical design of the three IRC channels. The light from the telescope is split by the germanium beam splitter and the transmitted light is introduced to the NIR channel. The reflected light goes to the MIR-S. Figure 5 shows the transmission and reflectance of the beam splitter. The transmission was measured at 4.2 K in normal incidence. The shift in the wavelength for the 45 degree incidence was estimated from the transmission measurement at room temperature between the normal incidence and the 45 degree incidence. The reflectance was simply estimated from the transmission, which was confirmed by the re-

**Table 1.** IRC band characteristics

(1)	(2)	(3)	(4)	(5)	(6)	(7)	(8)
Channel*	Name	element	$\lambda_{\text{ref}}$	Wavelength	$\lambda_{\text{iso}}$	$\Delta\lambda$	Dispersion
(pixel scale)			( $\mu\text{m}$ )	( $\mu\text{m}$ )	( $\mu\text{m}$ )	( $\mu\text{m}$ )	( $\mu\text{m}/\text{pix}$ )
(1."46 $\times$ 1."46)	N2	filter	2.4	1.9–2.8	2.34	0.71	—
	N3	filter	3.2	2.7–3.8	3.19	0.87	—
	N4	filter	4.1	3.6–5.3	4.33	1.53	—
	NP	prism		1.8–5.5	—	—	0.06 @3.5 $\mu\text{m}^\dagger$
	NG	grism		2.5–5.0	—	—	0.0097
(2."34 $\times$ 2."34)	S7	filter	7.0	5.9–8.4	7.12	1.75	—
	S9W	filter	9.0	6.7–11.6	8.61	4.10	—
	S11	filter	11.0	8.5–13.1	10.45	4.12	—
	SG1	grism		4.6–9.2	—	—	0.057
	SG2	grism		7.2–13.4	—	—	0.097
(2."51 $\times$ 2."39)	L15	filter	15.0	12.6–19.4	15.58	5.98	—
	L18W	filter	18.0	13.9–25.6	18.39	9.97	—
	L24	filter	24.0	20.3–26.5	22.89	5.34	—
	LG2	grism		17.5–26.5	—	—	0.17

(4) Reference wavelength.

(5) Defined as where the responsivity is larger than  $1/e$  of the peak for the imaging mode.

See Ohyama et al. (2007) for the spectroscopic modes.

(6) Isophotal wavelength of the filter band for Vega.

(7) Effective bandwidth.

\* All the channels have fields-of-view of about  $10' \times 10'$  (see Fig. 3).

$^\dagger$  Dispersion power of NP depends on the wavelength.

flectance measurement at room temperature. As can be seen in the figure, the transmission is better than the requirement of 70% across most of the spectral range below  $12 \mu\text{m}$ . However the beam splitter is not perfect in any sense and in fact produces ghost images by reflections within it particularly at wavelengths where the transmission becomes worse ( $> 12 \mu\text{m}$ , see below). The dip at  $3.4 \mu\text{m}$  is seen exactly at the same wavelength in the system throughput of the NIR spectroscopic modes (Ohyama et al. 2007), providing an independent confirmation of the transmission curve of the beam splitter. The cold stop is located right behind the filter wheel as shown in figure 4 for all three channels. Details of the optical and mechanical design of the NIR channel are given in Kim et al. (2005). The NIR consists of silicon and germanium lenses. There are non-negligible color aberrations between the N2 and the N3/N4 bands, which were utilized for the telescope focus adjustment (Kaneda et al. 2007). They are smaller than the

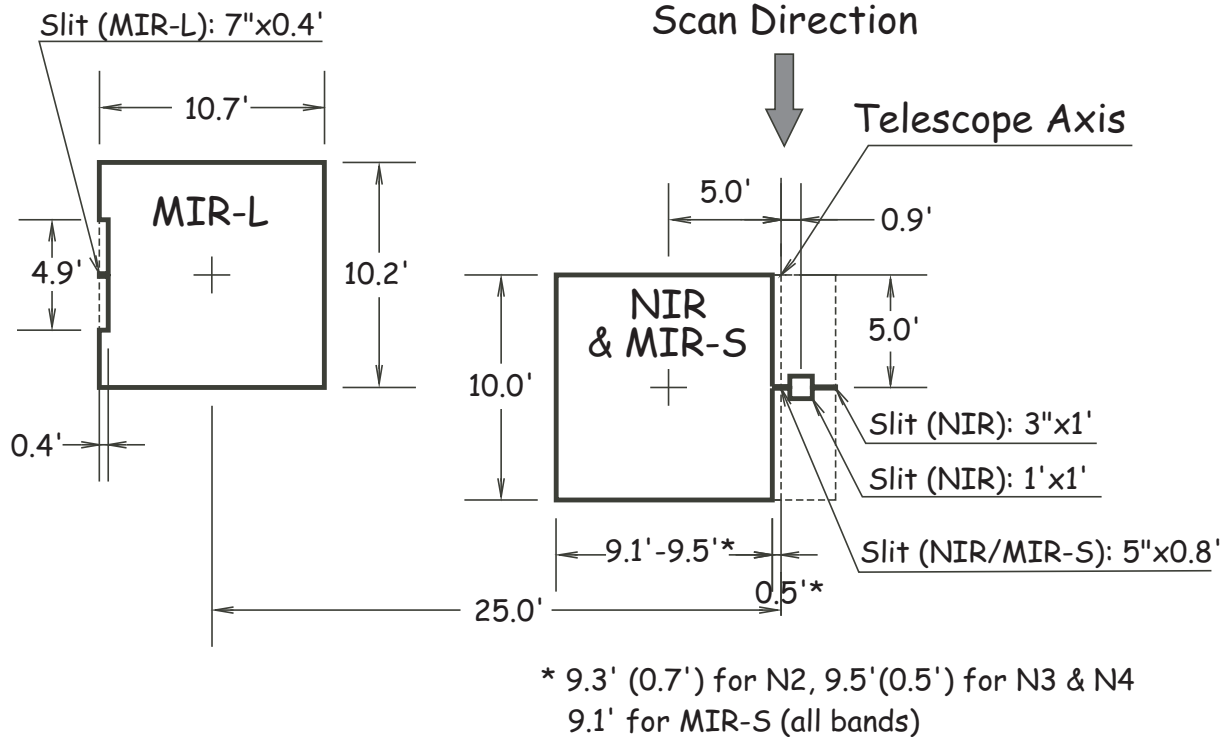


**Fig. 3.** Field-of-view location of the three IRC channels. The vertical arrow indicates the scan direction in the survey mode. The NIR and MIR-S share the same field-of-view by means of the beam splitter. See text for the NIR slit usage.

wave-front errors of the telescope, which dominate in the total wave-front errors for the NIR channel. The NIR has a prism consisting of silicon and  $\text{CaF}_2$  and a germanium grism as the dispersers. The grism provides medium resolution spectroscopic capability in the near-infrared. The pixel scale of the NIR channel is  $1.''46$ .

The MIR-S channel optics consist of two aspherical germanium lenses. It has two medium band filters (S7 and S11) and a wide-band filter (S9W), the latter of which is used for deep survey as well as for the all-sky survey observations. It also has two grisms of KRS-5 to cover the wavelength range  $4.6$  to  $13.4\mu\text{m}$ . The pixel scale of the MIR-S channel is  $2.''34$ .

The MIR-L has the most complicated optical design: It has a cylindrical pick-up mirror to correct for astigmatism. The MIR-L channel consists of 3 CsI and 2 KRS-5 lenses. Because of the cylindrical mirror, the pixel scale is different in the orthogonal directions, being  $2.''51 \times 2.''39$ . The scale in the horizontal direction of Figure 3 is longer than that in the vertical direction. Details of the MIR-L design are given in Fujishiro et al. (2005). The MIR-L has two medium-band filters (L15 and L24) and a wide-band filter (L18W), the latter of which is used for the deep survey as well as the all-sky survey observations. The MIR-L had two grisms of KRS-5, but one of them (LG1), which was designed to cover the  $11\text{--}19\mu\text{m}$  spectral range, became opaque in the last stage of ground testing and the spectroscopic capability between  $13\text{--}18\mu\text{m}$  was lost. Part of the edges of the spectral range of LG1 are covered by SG1 and LG2 (see



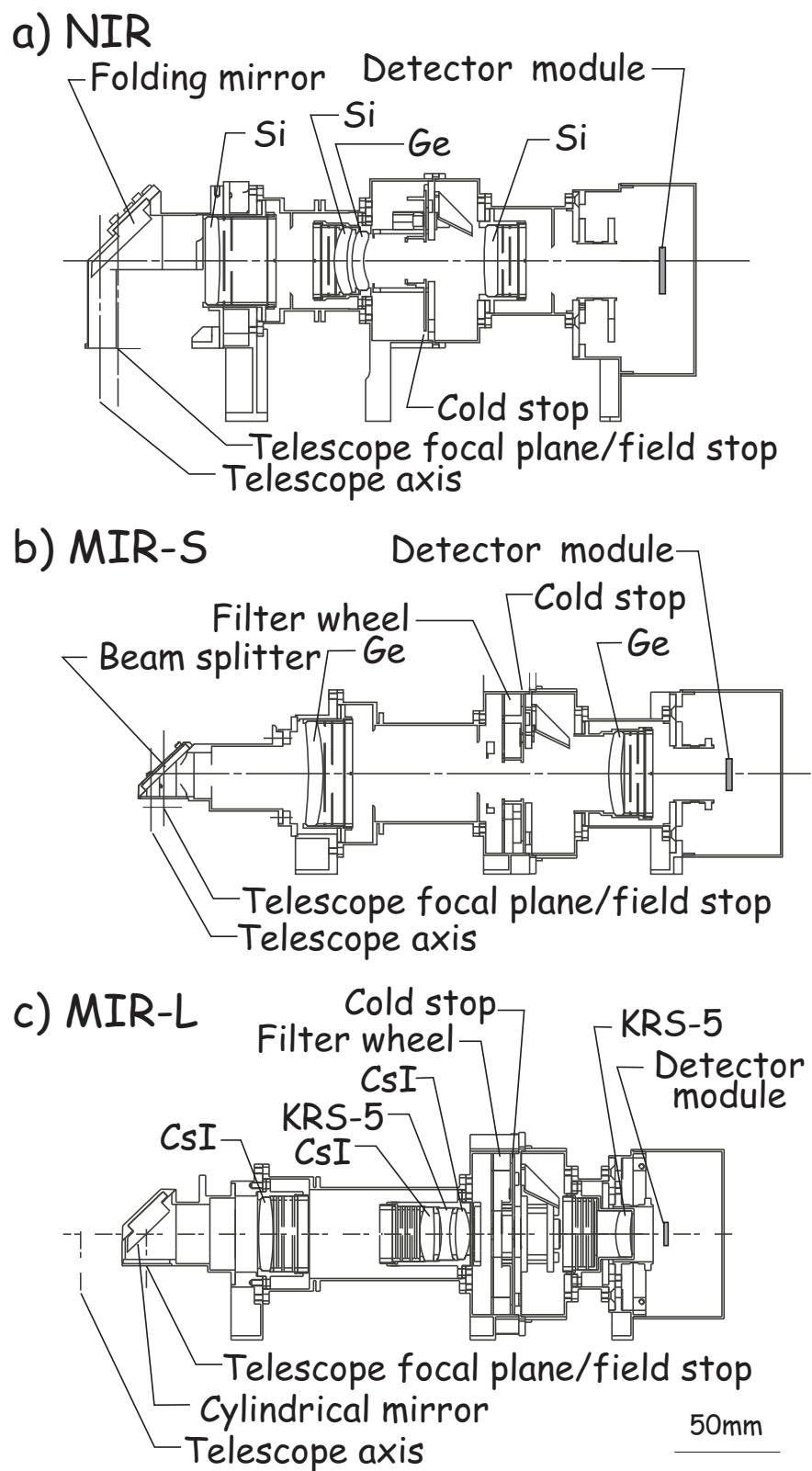


**Fig. 4.** Side-view of the IRC three channels. a) NIR, b) MIR-S, and c) MIR-L.



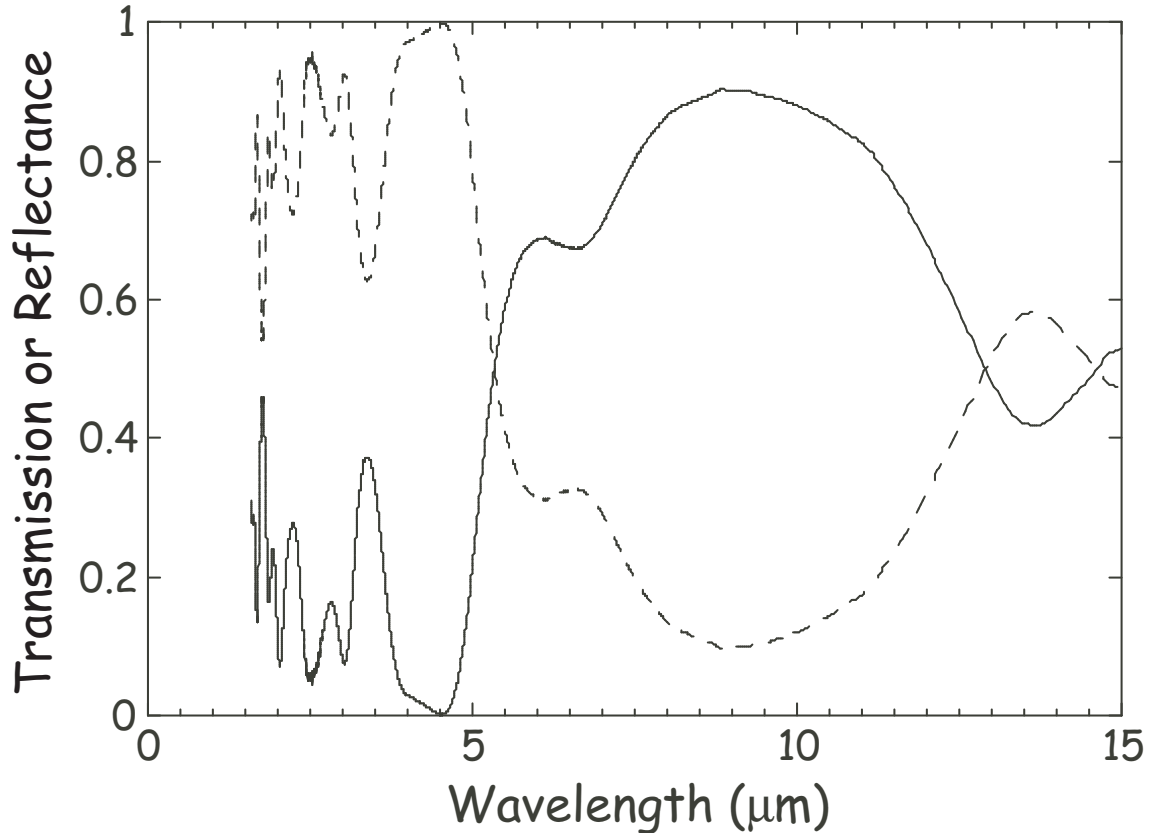


**Fig. 5.** Transmission and reflectance of the beam splitter at 4.2 K. The dashed line indicates the transmission and the solid line the reflectance. See text for details.

Table 1).

The warm electronics of IRC is installed in the same electronics box as the other on-board scientific instrument, the Far-Infrared Surveyor (FIS; Kawada et al. 2007). The electronics box is thermally insulated and attached to the outer shell of the cryostat (Nakagawa et al. 2007). It controls the array operation, takes signals, and sends them to the Data Handling Unit (DHU) of the spacecraft. It also receives the signal of the attitude stability for the pointing observation, which initiates the array operation sequence. The warm electronics of IRC consists of the power supply, the array drivers, the peripheral control, the sequencer, and the on-board computer unit (CPU) boards. The clock pattern for the array operation is sent to the sequencer by a trigger from the CPU. The array operation is carried out by the sequencer independently and thus it is not affected by the CPU status. Details of the IRC electronics and the array operations are given in Wada et al. (2003) and Ishihara et al. (2006a).

### 3. Focal-plane array operation and observation mode

In the pointing mode, a combination of the exposure, filter exchange, and dithering operations is fixed to several patterns, which are called Astronomical Observation Template

(AOT). The IRC AOT is designated as IRCxx, where xx indicates the AOT number. The IRC AOT in use for actual astronomical observations includes one-filter mode (IRC05), two-filter mode (IRC02), three-filter mode (IRC03), spectroscopic mode (IRC04), and slow-scan mode (IRC11 and IRC51). IRC05 was chosen on orbit to be used as the one-filter mode, for which IRC00 was originally planned. Since IRC00 has rarely been used on orbit, only IRC05 is described in the present paper. In each AOT, there are additional parameters for the selection of filters, dispersers, field-of-view location, and usage of the slit.

A unit of the exposure pattern of the focal-plane array is the same for all the AOTs except for IRC05. The unit is called ‘exposure frame’. The unit frame except for IRC05 is called a standard frame. The unit exposure frame for IRC05 is defined as an IRC05 frame and is described separately. The operation of the MIR-S and MIR-L arrays is controlled by the same clock and thus has the same exposure pattern (Wada et al. 2003). It takes about 70s to execute one standard frame. One standard frame consists of short and long exposures as shown in figure 6a. The short exposure is accommodated to increase the dynamic range: One standard frame of the NIR channel consists of one short exposure and one long exposure and the short exposure time is 1/9.5 of the long exposure frame. One standard frame of the MIR-S and MIR-L channels has one short exposure and three long exposures and the short exposure time is 1/28 of the long one. Data of each array are taken using a Fowler sampling method (Fowler & Gatley 1990). The Fowler sampling method consists of N non-destructive reads immediately after the reset (pedestal reads) and another N non-destructive reads near the end of the integration (signal reads). The average of pedestal reads is subtracted from the average signal reads on board and transmitted to the ground. In the short exposure, the data are taken with Fowler 1 sampling. The Fowler 4 sampling is employed for the long exposure in the standard frame. The IRC05 frame time is twice as long as the standard frame to enable the Fowler 16 sampling for NIR deep observations with one filter as shown by  $Fr^*$  in figure 6b. One IRC05 frame has two standard frames of MIR-S and MIR-L.

A set of frames is arranged to accommodate each AOT. Including the time for the filter exchange and dithering operations, one pointed observation has 8 to 9 frames for IRC02, IRC03, and IRC04, and 4 or 5 frames for IRC05. Figure 6c shows a schematic diagram of the operations in four IRC AOTs. For IRC02, dithering operation is executed every two frames with different filters. For IRC03, three frames with three different filters are taken, followed by one dithering operation. In the IRC04 sequence, there is no dithering operation. After four consecutive frames with the same dispersive element, one reference image frame is taken, and then another set of frames with another dispersive element is taken. The reference image is used to derive the wavelength reference position (see Ohyama et al. 2007 for details). IRC05 does not have any dithering or filter change operations.

In a pointed observation, there is also one exposure frame before and after each pointed observation of the target during the satellite maneuver, in which the filter wheel is positioned

at the shutter (pre- and post-dark frame). For IRC11 and IRC51, measurements with the shutter closed are also made during the maneuver. Except for IRC02, more than two pointed observations are recommended to obtain at least three images of science targets for reliability and rejection of high-energy ionization particle hits particularly for NIR observations since only one or two frames of the same filter/disperser are taken with AOTs other than IRC02.

The slow scan AOTs, IRC11 and IRC51, are designed to observe a relatively wide area ( $\sim 1^\circ$  strip) in one pointed observation. The satellite moves continuously with a slow rate of a fixed pattern. The same array operation used for the all-sky survey mode is employed in these observations (Ishihara et al. 2006a). Only the data for two rows of each of the MIR-S and MIR-L arrays are taken because of the limitations of the data downlink capacity and the array drive electronics. In IRC11, the data of 4 pixels in the cross-scan direction are binned together in the same manner as in the all-sky survey observation to reduce the rate of the data produced (see § 4.8), while no binning is made for IRC51. As long as the downlink capacity is allowed, IRC51 is employed for IRC slow scan observations. Details of the in-flight operation of IRC51 are given in Ishihara et al. (2007).

## 4. In-flight performance

IRC is working without any degradation on orbit and the in-flight performance has been confirmed to be within the pre-flight expectation.

### 4.1. System throughput

The spectral throughput in units of electrons per photon of the imaging bands was estimated on the basis of laboratory measurements of each optical element. It is proportional to the detector quantum efficiency. It was confirmed by end-to-end measurements of IRC without the telescope in the laboratory except for the MIR-L, for which the end-to-end test was not able to be carried out (Onaka et al. 2004). The final system throughput is scaled by the in-flight absolute calibration and is shown in Figure 7. There are small red leaks in the N2 ( $<1.8\%$ ) and N3 ( $<1\%$ ) bands around  $5\mu\text{m}$ . Blue leaks in MIR-S and MIR-L shorter than 4 and  $10\mu\text{m}$ , respectively, are recognizable, but they are all less than  $0.01\%$ . The system throughput for the spectroscopic mode is given in Ohyama et al. (2007), which was derived from in-flight data. It also basically agrees with pre-flight laboratory measurements.

### 4.2. Calibration and stability

The in-flight absolute calibration of IRC is made by observations of standard stars prepared on the basis of the same standard star networks as *MSX* and *IRAC*, which assures that the IRC calibration is tied with *IRAC* and other facilities whose calibration is based on the same networks (Cohen et al. 1999; Cohen et al. 2003; Ishihara et al. 2006b). At present the accuracy of the absolute calibration for pointed observations is estimated to be better than  $5\%$

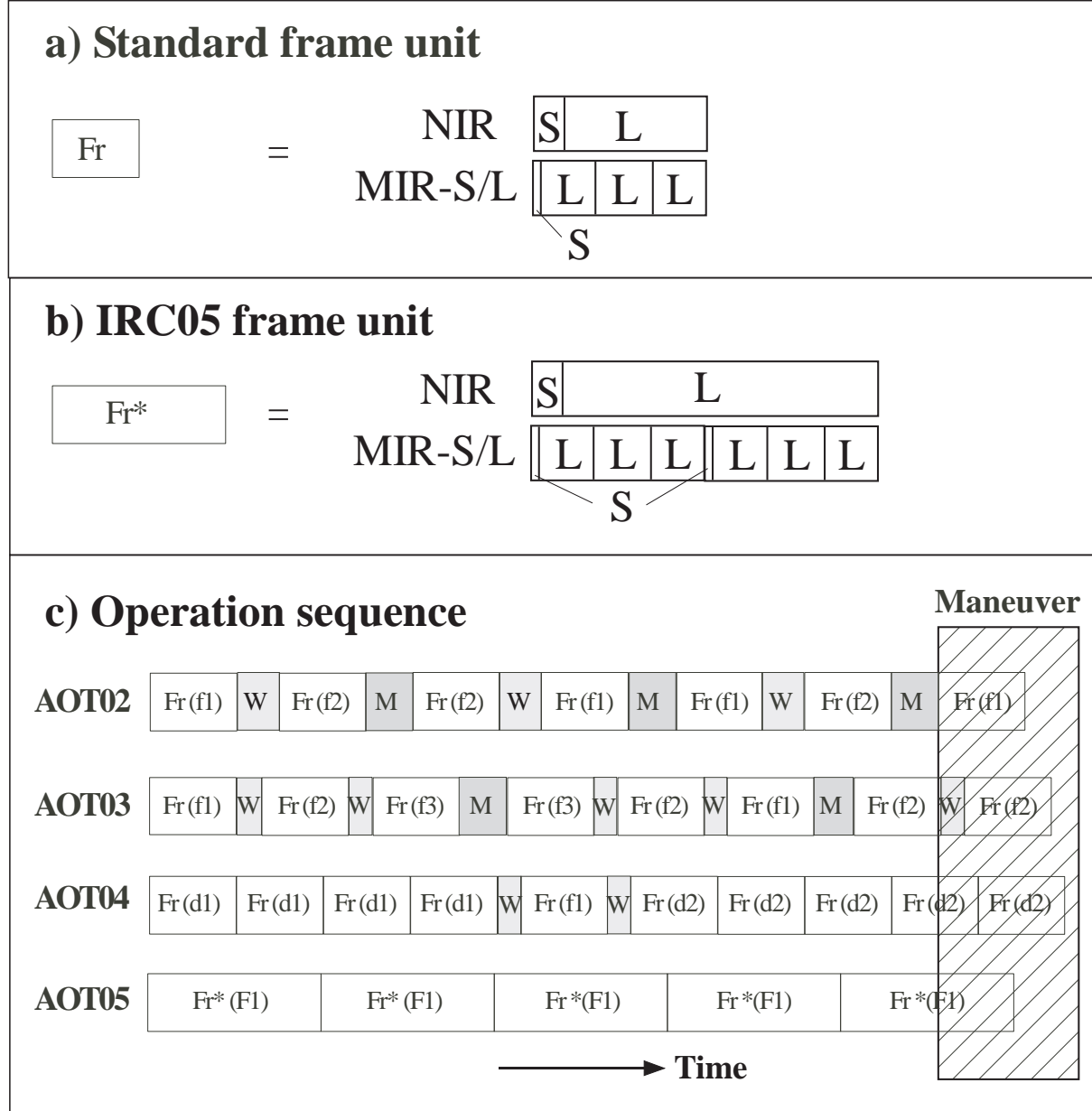


**Fig. 6.** Unit frame and operation sequence of the major IRC AOTs used on orbit. (a) Standard frame unit ( $Fr$ ) and (b) IRC05 frame unit ( $Fr^*$ );  $L$  indicates the long exposure and  $S$  shows the short exposure. (c) Operation sequences for four IRC AOTs. The boxes with  $Fr$  and  $Fr^*$  show standard frames and IRC05 frames, respectively, in which  $f\#$  and  $d\#$  in the parentheses indicate the filter and dispersive element, respectively. The boxes with  $M$  indicate a dithering operation, whereas  $W$  shows a filter wheel operation. The shaded boxed in the right indicates the region, in which the satellite maneuver may be carried out and thus the frames may be taken while the target is moving. Whereas the duration of one exposure frame is well fixed, the operation time for the filter wheel and dithering depends on the relative positions of the wheel and the attitude control system. Hence the length of the box is not very accurate.

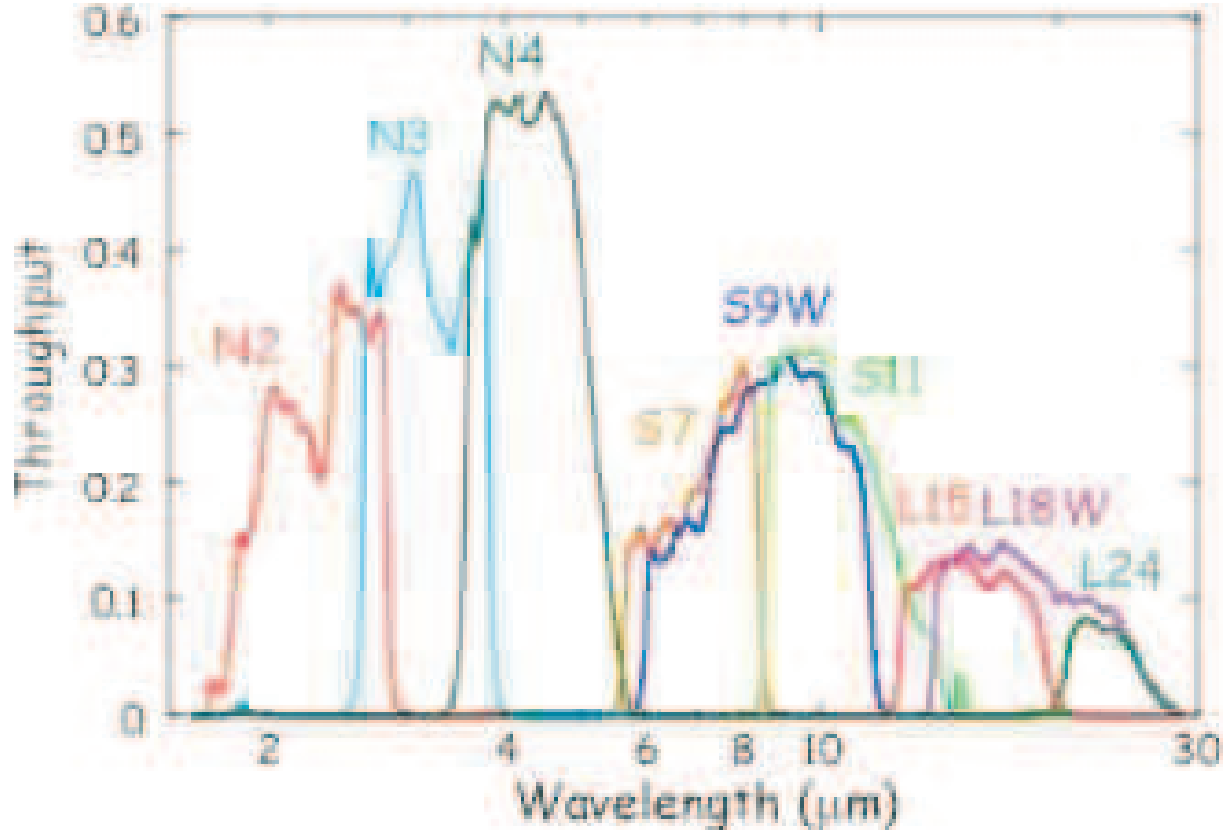


**Fig. 7.** System throughput of the IRC imaging bands (electrons per photon).

except for L24, for which it is about 6%. The calibration of the flux density for a source is made at the reference wavelength  $\lambda_{\text{ref}}$  (4th column of Table 1) for a nominal spectrum of  $\nu I_{\nu} = \text{const.}$  A color correction table for various spectra is given in the IRC Data User's Manual (Lorente et al. 2007).

The stability of the system response has been investigated on the basis of monitoring observations of the same stars in the continuous visibility regions every one to two weeks. No systematic trends have so far been seen over a half year. The system response is found to be stable within 5% for all the imaging modes. The frequency of the monitoring observations will be reduced owing to the excellent stability of IRC.

#### 4.3. Image quality and sensitivity

The image size of the IRC is estimated on the basis of a number of stellar images. Average values of the FWHM of the image size are summarized in Table 2. The image quality of the NIR channels is limited by the wave-front errors of the telescope, but part of the image quality of the NIR channels can also be attributed to the color aberrations and the pointing stability of the satellite. The image size in the L24 band is slightly larger than the predicted performance. The reason is not known at present.

**Table 2.** IRC sensitivity and image quality

Band	5- $\sigma$ sensitivity*			Saturation <sup>†</sup>	Image quality	
	per pointing ( $\mu$ Jy)			level	FWHM	Peak central
	AOT02	AOT03	AOT05	(Jy)	(arcsec)	pixel flux (%)
N2	16	20	5 <sup>‡</sup>	0.8	4.3	5.9
N3	16	19	5 <sup>‡</sup>	0.6	4.0	5.9
N4	16	19	9 <sup>‡</sup>	0.4	4.2	5.7
S7	74	91	43	4.3	5.1	12.0
S9W	76	93	44	2.7	5.5	11.5
S11	132	162	76	3.7	4.8	12.1
L15	279	341	161	9.9	5.7	7.9
L18W	273	335	158	8.4	5.7	6.6
L24	584	716	337	70	6.8	4.1

\* For low background. The effective on-source time per filter is 130, 90, 260s for NIR and 150, 100, and 440s for MIR-S and MIR-L, for AOT02, AOT03, and AOT05, respectively.

<sup>†</sup> The saturation level for the short exposure (see text).

<sup>‡</sup> The values for N2, N3, and N4 of IRC05 are tentative.

The point-source sensitivity per one long exposure is estimated from the aperture photometry of stars in low background regions. The aperture size is chosen to maximize the signal-to-noise (S/N) ratio by taking account of the point spread function (PSF). The sensitivity for each AOT in one pointed observation is simply scaled from the estimate per long exposure. The sensitivity of the NIR bands for IRC05 are estimated separately. The 5- $\sigma$  sensitivities per pointing are summarized also in Table 2. The effective on-source time is given in a footnote of the table. Also the saturation level for the short exposure is estimated at the flux at which the error in the linearity correction becomes 5% at the central pixel (see next subsection) and is listed also in the table. For MIR-S and MIR-L, the sensitivity is limited by shot noise from the sky background. The sensitivity on orbit is in agreement with the pre-flight estimation within 20–30%.

#### 4.4. Distortion and linearity

The image distortion is estimated from observations of stars in globular clusters except for L24 and those in a region near the Galactic center for L24. At present the accuracy in the distortion correction is about 0.1 pixel except for L24, for which it is about half a pixel. The worse value for L24 comes mainly from the small number statistics, the scarcity of bright sources in a field-of-view of the MIR-L.

Because of the debias effects during an integration, an appreciable non-linearity exists for signals of all the IRC detectors. Polynomial fits up to the 7th order are used to correct for it. After the correction, the error from the ideal linearity is better than 5% at 12000, 20000, and 20000 analog-to-digital units (ADUs) for NIR, MIR-S, and MIR-L, respectively. The physical detector saturation occurs at about 125000, 33000, and 33000 ADUs for NIR, MIR-S, and MIR-L, respectively.

#### 4.5. *Dark and flat field*

Pre- and post-dark frames before or after a pointed observation can be used as the dark frame. Post-dark frames occasionally show latent images from pointed observations and cautions have to be given when they are used as the dark frame. The pre-dark image does not have a high S/N ratio. It is particularly true for the NIR, for which the pre-dark data consist of only one long exposure. To have dark images of high S/N ratios, ‘superdark’ images were created from a number of pre-dark frames taken in the early phase of the mission. The dark signals are found to vary after passage of the South Atlantic Anomaly. Thus the temporal variation must be corrected when the superdark is used. This can be done by taking account of the offset between the superdark and the dark signal before the target observation for the region masked by the field stop. The superdark images have the advantage of a high S/N ratio for the pixel-to-pixel variation, however, they do not correct for the increased dark signal of a band-like pattern due to the IRC all-sky survey observation in the MIR-S and MIR-L channels. They also do not accommodate the increasing number of hot pixels. Users have a choice which dark data are used for the data reduction. The superdark is prepared mainly for the dark estimate for NIR and for observations whose pre-dark measurement failed.

For the NIR bands, the flatfield library was made from observations of the north ecliptic pole (NEP). Since the sky is very faint in the near-infrared, the S/N ratio is about 5 for N2 and N3, and 10 for N4 at present.

For the MIR channels, the flatfield library was made from observations of the ecliptic plane (EP). The S/N ratios for the MIR-S and MIR-L bands are about 100. The flat image of MIR-L shows a noticeable pattern, which shows a large gradient ( $\sim 30\%$ ) at the edges. It is surmised that the flatfield for the MIR-L bands is affected by scattered light, which presumably originates from internal reflections inside the MIR-L channel. Part of the flatfield pattern can be attributed to the scattered light. The current estimate suggests that the flatfield for the MIR-L channels may have an error of 10% on a large spatial scale due to the scattered light effect.

#### 4.6. *Artifacts of the arrays*

The IRC arrays show similar artifacts to those known for the IRAC arrays, such as multiplexer bleed, column pull-down, and banding (Fazio et al. 2004). Details are described in the IRC Data User’s Manual (Lorente et al. 2007). So far, latent images do not seem to be a



serious problem probably because the arrays are switched to the all-sky survey mode and kept continuously running after the pointed observation. The scattering inside the arrays (banding) is under investigation and calibration for extended sources is being planned as done by Cohen et al. (2007) for IRAC.

#### 4.7. *Ghosts and scattered light*

The NIR and MIR-S channels are known to have ghosts originating from the reflection in the beam splitter. They are most noticeable in the S11 with a level of 4%. For other NIR and MIR-S bands, they are less than 1%. These ghosts are well predictable in position and intensity and thus can be corrected.

There are several kinds of known scattered light in IRC images. The first kind is that seen only in the periphery of the MIR array detectors. It is thought to originate from the scattering at the detector edge. An extensive study of the MIR-S array has shown that it is very stable and thus correctable (Sakon et al. 2007).

Due to the short baffle of the telescope tube, it was predicted that the light scattered off the top of the reflective baffle could come into the telescope at particular seasons of the observation. This scattered light is recognized in some IRC images. The effect of this scattered light on the flatfields is carefully examined by selecting less-affected data and minimized. This scattered light does not affect observations of point sources significantly. However, observations of diffuse background light are severely affected and need a special caution.

The most serious problem in the IRC calibration at present is the internal scattering light inside the MIR-L channel. It is largely noticeable at L24. It affects the flatfield of the MIR-L channels to a level of 10% as described above. Ghost images, which might also be related to this scattered light, are seen against very bright mid-infrared sources. Characterization of this component is now under investigation.

#### 4.8. *All-sky survey observation*

Two wide bands of S9W and L18W are used for the IRC mid-infrared all-sky survey observations. Only the data of two rows of the MIR-S and MIR-L arrays are taken in the all-sky survey mode and signals of 4 pixels in the cross-scan direction are binned on board and transmitted to the ground (Ishihara et al. 2006a). Reading two rows helps in rejecting spurious signals and high-energy ionization particle hits, and thus significantly increases the reliability of source detection. The virtual pixel scale is about  $10'' \times 10''$  for both bands. The two rows are read in an interlaced manner to increase the spatial information.

The absolute calibration of the all-sky survey observation is carried out similarly on the basis of observations of stars of the same standard star network on orbit (Ishihara et al. 2007). At present, the accuracy in the absolute calibration is estimated to be 7 and 15% for S9W and L18W, respectively. The  $5\text{-}\sigma$  sensitivity for point source detection in a scan is confirmed to be about 50 mJy at S9W and 120 mJy at L18W. In the all-sky survey, the sensitivity is limited

by detector noise in both bands. These numbers are well in agreement with the pre-flight expectations as well as the in-orbit sensitivity for pointed observations. The IRC mid-infrared all-sky survey observation achieves a deeper sensitivity and a finer spatial resolution by about an order of magnitude than the *IRAS* 12 and 25  $\mu\text{m}$  survey. Potential capabilities of the IRC all-sky survey to extragalactic sciences are discussed in Pearson et al. (2004) and Pearson et al. (2007).

## 5. Summary

IRC is one of the two instruments on *AKARI* satellite. It has an imaging capability in the spectral range 1.8 to 26.5  $\mu\text{m}$  with 9 photometric bands and makes wide-field deep imaging in pointed observations. It also has a low-resolution spectroscopic capability, which allows slit-less multi-object spectroscopy in the near to mid-infrared. IRC is being used also in an all-sky survey observation mode at 9 and 18  $\mu\text{m}$  with a higher sensitivity and better spatial resolution by an order of magnitude than the *IRAS* 12 and 25  $\mu\text{m}$  survey. It has been confirmed that the in-orbit performance of IRC is well within the pre-launch predictions and that IRC will provide significant data in various fields of cutting-edge astronomy. IRC data are now being processed with the pipeline software that takes account of the basic calibrations. Details are described in the IRC Data User's Manual (Lorente et al. 2007). Examples of IRC data are shown in this issue, which indicate the great potential of IRC observations. The NIR channel is planned to continue observations after the exhaustion of liquid helium.

*AKARI* is a JAXA project with the participation of ESA. We thank all the members of the *AKARI* project for their continuous help and support. We thank T. Negishi, I. Maeda, H. Mochizuki, K.-W. Chan, S. Fujita, and C. Ihara for their contributions in the development of the IRC and D. Jennings for providing us with the on-board calibration sources. We also thank K. Imai, M. Ishigaki, H. Matsumoto, N. Matsumoto, and T. Tange for supporting daily operation of the IRC. The contribution from the ESAC to the pointing reconstruction is greatly acknowledged. W.K., I.S., and T.T. have been financially supported by the Japan Society of Promotion of Science (JSPS). This work is supported in part by a Grant-in-Aid for Scientific Research on Priority Areas from the Ministry of Education, Culture, Sports, Science, and Technology of Japan and Grants-in-Aid for Scientific Research from the JSPS.

## References

- Cesarsky, C. J., et al. 1996, *A&A*, 315, L32
- Cohen, M., et al. 1999, *AJ*, 117, 1864
- Cohen, M., Megeath, T. G., Hammersley, P. L., Martin-Luis, F., & Stauffer, J. 2003, *AJ*, 125, 2645
- Cohen, M., et al. 2007, *MNRAS*, 374, 979
- Fazio, G. G., et al. 2004, *ApJS*, 154, 10

Fowler, A. M., & Gatley, I. 1990, ApJL, 353, L33  
 Fujishiro, N., et al. 2005, Proc. SPIE, 5904, 154  
 Ishihara, D., et al. 2006, PASP, 118, 324  
 Ishihara, D., et al. 2006, AJ, 131, 1074  
 Ishihara, D., et al. 2007, PASJ, submitted  
 Houck, J. R., et al. 2004, ApJS, 154, 18  
 Kaneda, H., et al. 2007, PASJ, submitted  
 Kawada, M., et al. 2007, PASJ, submitted  
 Kim, W., et al. 2005 Proc. SPIE, 5904, 378  
 Lorente, R., Onaka, T., Ita, Y., Ohyama, Y., & Pearson, P. 2007, AKARI IRC Data User Manual  
 ver.1.1, <http://www.ir.isas.jaxa.jp/AKARI/Observation/>  
 Murakami, H., et al. 2007, PASJ, submitted  
 Matsuhara, H. Shibai, H., Onaka, T., & Usui, F. 2005, Adv. Sp. Res. 36, 1092  
 Matsuhara, H., et al. 2006, PASJ, 58, 673  
 Neugebauer, G., et al. 1984, ApJL, 278, L1  
 Nakagawa, T., et al. 2007, PASJ, submitted  
 Ohyama, Y., et al. 2007, PASJ, submitted  
 Onaka, T., et al. 2004, Proc. SPIE, 5487, 338  
 Pearson, C. P., et al. 2004, MNRAS, 347, 1113  
 Pearson, C. P., et al. 2007, PASJ, submitted  
 Sakon, I., et al. 2007, PASJ, submitted  
 Wada, T., et al. 2003, Proc. SPIE, 4850, 179  
 Watarai, H., et al. 2000, Proc. SPIE, 4013, 59